Vibrationally Resolved Photoionization Delays in the Water Molecule

Prateek Pranjal,[1] Jesus González-Vázquez,[2] Roger Y. Bello,[3,*] and Fernando Martín[1,2,†]
[1]Instituto Madrileño de Estudios Avanzados en Nanociencia (IMDEA-Nanociencia), Cantoblanco, 28049, Madrid, Spain
[2]Departamento de Química, Módulo 13, Universidad Autónoma de Madrid, 28049 Madrid, Spain
[3]Departamento de Química Física Aplicada, Universidad Autónoma de Madrid, 28049, Madrid, Spain

(Received 17 March 2025; revised 28 August 2025; accepted 6 November 2025; published 26 November 2025)

We have implemented a theoretical approach to provide time- and vibrationally resolved photoelectron spectra and ionization time delays of polyatomic molecules as those expected from current high energy resolution reconstruction of attosecond beatings by interference of two-photon transitions setups. Its application to the H_2O molecule reveals that two-photon ionization delays extracted from the calculated photoelectron spectra do not vary monotonically with photon energy and can increase or decrease along the vibrational progressions. The difference between one- and two-photon ionization delays is substantially larger when the molecular cation is left in the symmetric stretching mode (up to 35 as, i.e., comparable to the actual ionization delays) rather than in the bending mode, thus showing a strong vibrational selectivity in the laser-photoelectron interaction. Hence, the variation of calculated two-photon delays with the final vibrational state does not simply reflect the energy dependence of the Coulomb phases, as usually assumed in a structureless electronic continuum, but also the changes in the molecular geometry associated with the different vibrational modes. As vibrational excitation accompanying the emission of a photoelectron is the rule rather than the exception in polyatomic molecules, the present Letter shows the importance of considering nuclear motion for a correct interpretation of ionization time delays.

DOI: 10.1103/jzfm-8vhj

The time an electron takes to escape from an atom or a molecule after absorption of an extreme ultraviolet (XUV) photon is usually very short, of the order of tens or few hundreds of attoseconds. Measuring these photoionization times has become standard practice in attosecond science since its early days by using either electron streaking [1,2] or two-photon interferometric approaches. Among the latter, reconstruction of attosecond beatings by interference of two-photon transitions (RABBIT) [3] is the most widely employed method to date. Photoionization times are intimately linked to the electronic structure of the system and the potential landscape that the ionized electron sees in its way out. For this reason, they can provide valuable information complementary to that obtained from more classical spectroscopic approaches in the energy domain.

RABBIT has amply been used to determine two-photon ionization times in atomic systems (see, e.g., Refs. [4–15] and references therein) and more recently in molecules [16–28]. In the latter case, they have been shown to be sensitive to the presence of shape [17,21,23,29,30] or Feshbach [16,19,25,27] resonances in the electronic continuum, to the anisotropy of the molecular potential arising from its multicenter character [26], and even to nuclear motion, including vibration [21] and dissociation [28]. In many instances, these effects cannot be separated from each other. For example, in the vicinity of narrow Feshbach resonances, the nuclei may have enough time to move significantly before ionization takes place, which strongly affects ionization times [19,27]. Also, vibrations or breakup of particular chemical bonds can induce changes in the anisotropy of the molecular potential, which is reflected in the measured delays [21]. All this makes extraction of photoionization times and their interpretation challenging, requiring support from theoretical modeling in which both electronic and nuclear degrees of freedom are considered. However, with the exception of molecules with a single vibrational degree of freedom, H_2 [19,25,31], N_2 [21,27], and CH_4 in reduced dimensionality (1D) [28], interpretation of measured photoionization times is mostly based on the assumption that nuclei do not move (fixed-nuclei approximation, FNA) [17,18,22,32–34].

With the increasing energy resolution available in attosecond laboratories, RABBIT spectra can now provide vibrationally resolved information for diatomic molecules [16,21,27,31], which in conjunction with full dimensional theoretical methods, allows one to retrieve photoionization time delays resolved in both the photoelectron kinetic

*Contact author: roger.bello@uam.es
†Contact author: fernando.martin@uam.es

energy and the vibrational energy of the remaining molecular cation, thus offering new ways to understand the complex intertwining between electronic and nuclear motions. Getting a similar degree of understanding in polyatomic molecules is much more demanding due to the existence of several vibrational modes. In a recent attempt to include all nuclear degrees of freedom, Patchkovskii *et al.* [35–37] proposed to obtain RABBIT spectra from two-photon ionization matrix elements convoluted with vibronic cross-correlation functions. In contrast with that work, here we have implemented a time-dependent close-coupling approach that accounts for all electronic and vibrational degrees of freedom and directly provides time-resolved photoelectron spectra as those measured in high energy resolution RABBIT experiments.

Earlier RABBIT experiments on the H_2O molecule [17] have revealed the presence of structured harmonic (H) bands and sidebands (SB) in the photoelectron spectra, suggesting the presence of vibrational progressions, although the limited energy resolution available at that time did not allow for the extraction of vibrationally resolved information. In this Letter we have explored the same photon energy range as in Ref. [17] and retrieved vibrationally resolved photoionization times of the H_2O molecule from the calculated RABBIT spectra. Comparison with the experimental results of Ref. [17] after averaging over all accessible vibrational states is very good, thus validating our theoretical approach. More importantly, we show that, in two of the three accessible ionization channels, namely the $\tilde{X}^2B_1$ and $\tilde{A}^2A_1$ ones, the recorded SBs exhibit pure symmetric stretching and bending vibrational progressions, respectively. The extracted two-photon ionization delays (i) do not vary monotonically with photon energy, (ii) can either increase or decrease along the different vibrational progressions, and (iii) show a strong selectivity of the laser-photoelectron interaction with respect to the final vibrational mode, which is the consequence of geometrical changes associated with such modes.

To cover the whole range of photon energies considered in previous experimental work [17], we have used two different APTs as described in the End Matter section, where details of the theoretical method can also be found. Figure 1 shows the calculated photoelectron spectrum for one of the APTs at an XUV-IR delay of $\tau = 0.2$ fs [Fig. 1(b)], as a function of such delay [Fig. 1(c)], and after subtraction of the XUV-only spectrum [Fig. 1(d)]. The spectrum shows that, besides the harmonic bands associated with the absorption of the XUV photons, much less intense sidebands resulting from the additional absorption or emission of an IR photon appear in between consecutive harmonic bands [see also Fig. 1(a)]. As can be seen, harmonic bands and sidebands associated with the different ionization channels overlap in the same energy regions, leading to the usual spectral congestion characteristic of polyatomic molecules. The signature of the sidebands is

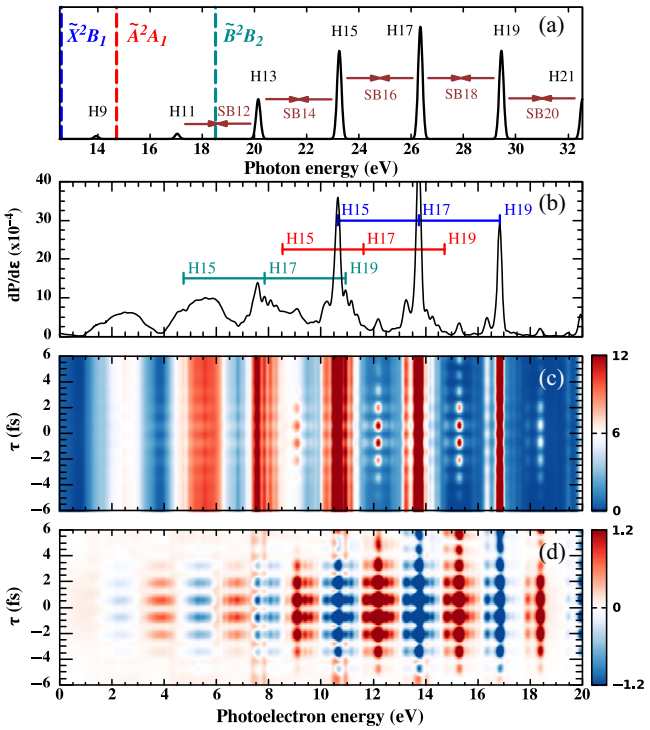

FIG. 1. (a) Fourier transform of the XUV pulse used in this Letter. (b) Photoelectron spectrum for an XUV-IR delay of 0.2 fs. (c) Photoelectron spectrum as a function of the XUV-IR delay, τ. (d) Difference spectrum, obtained by subtracting the XUV-only photoelectron spectrum from the XUV + IR one. Labels indicate the ionization thresholds for each channel, the harmonics (H), and the sideband orders (SB).

more apparent in Fig. 1(d) after subtraction of the XUV only spectrum. As expected, the sidebands oscillate with twice the frequency of the IR field, ω_{IR} [3], according to the following formula:

$$S(\tau) = A + B\,\cos\left(2\omega_{\mathrm{IR}}\tau - \Delta\phi_{\mathrm{mol}} - \Delta\phi_{\mathrm{XUV}}\right). \quad (1)$$

When the $\Delta\phi_{\mathrm{XUV}}$ phase difference due to the attochirp is known, this equation allows one to extract the intrinsic phase difference between the two interfering paths, $\Delta\phi_{mol}$, and hence the two-photon ionization delay $\tau_{\mathrm{mol}} = \Delta\phi_{\mathrm{mol}}/2\omega_{\mathrm{IR}}$. In our calculations, $\Delta\phi_{\mathrm{XUV}} = 0$.

Both harmonic bands and sidebands exhibit a rich vibrational structure. To better identify its origin and physical meaning, Fig. 2 shows the separate contributions of the $\tilde{X}^2B_1$, $\tilde{A}^2A_1$, and $\tilde{B}^2B_2$ ionization channels in the spectra integrated over the XUV-IR delays (top panel), as well as the spectra resulting from the subtraction of the corresponding XUV-only spectra (lower panels). In the latter, the signature of the different sidebands can be seen in the regions where the difference between the XUV + IR and XUV spectra is positive. The vibrational states are characterized by three quantum numbers (v_s, v_b, v_a), corresponding to the symmetric stretching, bending, and antisymmetric stretching vibrational motions, respectively.

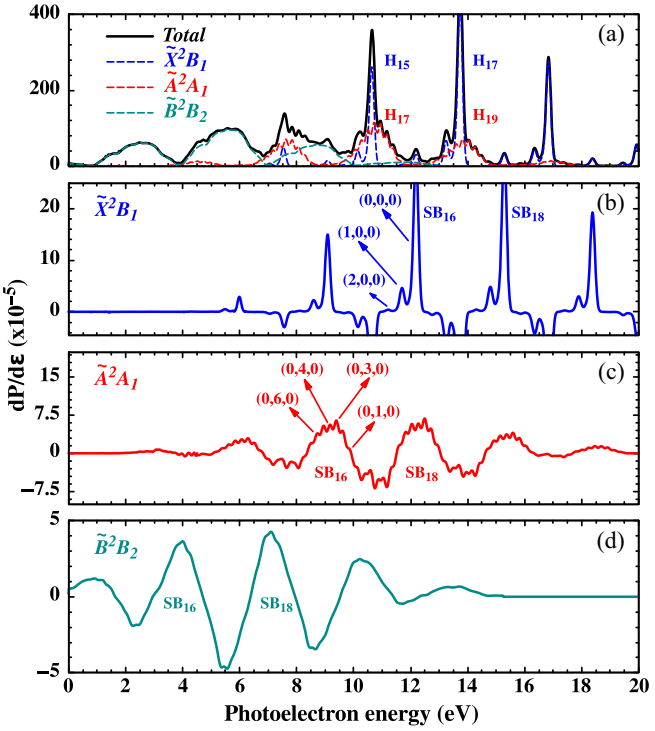

FIG. 2. Channel-resolved photoelectron spectrum for an XUV-IR delay of 0.2 fs. (a) Total and channel-resolved photoelectron spectra. (b)–(d) Difference spectra, obtained by subtracting the XUV-only photoelectron spectrum from the XUV + IR one for the $\tilde{X}^2B_1$, $\tilde{A}^2A_1$, and $\tilde{B}^2B_2$ channels, respectively. The notation (v_s, v_b, v_a) indicates the vibrational quantum numbers associated with the symmetric stretching, bending, and antisymmetric normal modes. Labels indicate the harmonics (H) and the sideband orders (SB).

Sidebands (as well harmonic bands) in the $\tilde{X}^2B_1$ channel exhibit a short vibrational progression in the symmetric stretching mode, which is dominated by the (0,0,0) peak with satellite contributions for the (1,0,0) and to a lesser extent the (2,0,0) vibrational states. This is the consequence of the fact that the geometry of the H_2O^+ cation in the minimum of the PES of the $\tilde{X}^2B_1$ state is similar to that of the X^1A_1 state of the neutral molecule (see, e.g., Ref. [38]). In contrast, sidebands associated with the $\tilde{A}^2A_1$ channel exhibit a long vibrational progression in the bending mode, ranging from (0,0,0) to (0,7,0) due to the different positions of the minima in the PES of the $\tilde{A}^2A_1$ and X_1A_1 states. The largest peak corresponds to leaving the cation in the (0,3,0) vibrational state. Contribution from the $\tilde{B}^2B_2$ channel to the spectrum is the smallest, and it is only visible at the lower photoelectron energies, below 8 eV. In this channel, the three vibrational modes contribute, with progressions in each individual mode and combinations of them. As a result, no individual vibrational peaks can be resolved. Although a direct comparison with the spectra reported in [17] is not possible because three different APTs were used in that work, the main features observed in the calculated spectrum nicely reproduce the experimental observations, notably the internal structure of the harmonic bands and sidebands, although here with much higher resolution.

To extract vibrationally resolved two-photon ionization delays, we have used Eq. (1) to fit the sidebands, for each vibrational state associated with each ionization channel, at their specific photon energies ($2n\hbar\omega_{IR}$). Note that, at a given photon energy, different vibrational states correlate to electrons with different energies according to energy conservation $2n\hbar\omega_{IR} = \varepsilon_\alpha + E_{\alpha v_\alpha}$, where ε_α and $E_{\alpha v_\alpha}$ are the photoelectron and vibrational energies associated with channel α, respectively. In Ref. [17], relative two-photon ionization delays, $\tilde{A}^2A_1 - \tilde{X}^2B_1$, were determined. Extraction of relative instead of absolute ionization times is so far the only way to discount the effect of the APT attochirp in RABBIT experiments. So, in order to compare with that experiment, we have also evaluated these relative ionization delays. As the experiment did not resolve the individual vibrational peaks, we have averaged our calculated relative delays over the whole vibrational progressions in the $\tilde{X}^2B_1$ and $\tilde{A}^2A_1$ sidebands. The results are shown in Fig. 3. The agreement with the experimental data is quite satisfactory. In particular, the theoretical results reproduce the nonmonotonic variation of the measured delays with photon energy, which pass from being positive ($\sim +25$ as) at the lower photon energies to negative at the higher photon energies (~ -15 as). The theoretical results predict that this nonmonotonic behavior is even more pronounced than the one expected from the available experimental data, especially between 22 and 28 eV, where unfortunately there are no experimental results. Remarkably, the observed variation of the two-photon delays does not follow that of the one-photon ionization delays, either in the FNA (also reported in [17]) or by including nuclear motion. In the FNA, the one-photon delay remains close to zero, and variations

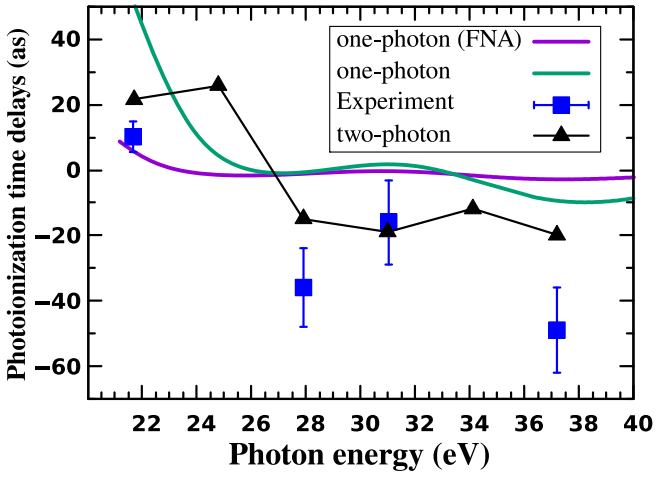

FIG. 3. Calculated and measured one- and two-photon relative $\tilde{A}^2A_1 - \tilde{X}^2B_1$ ionization delays. The experimental data were extracted from Ref. [17].

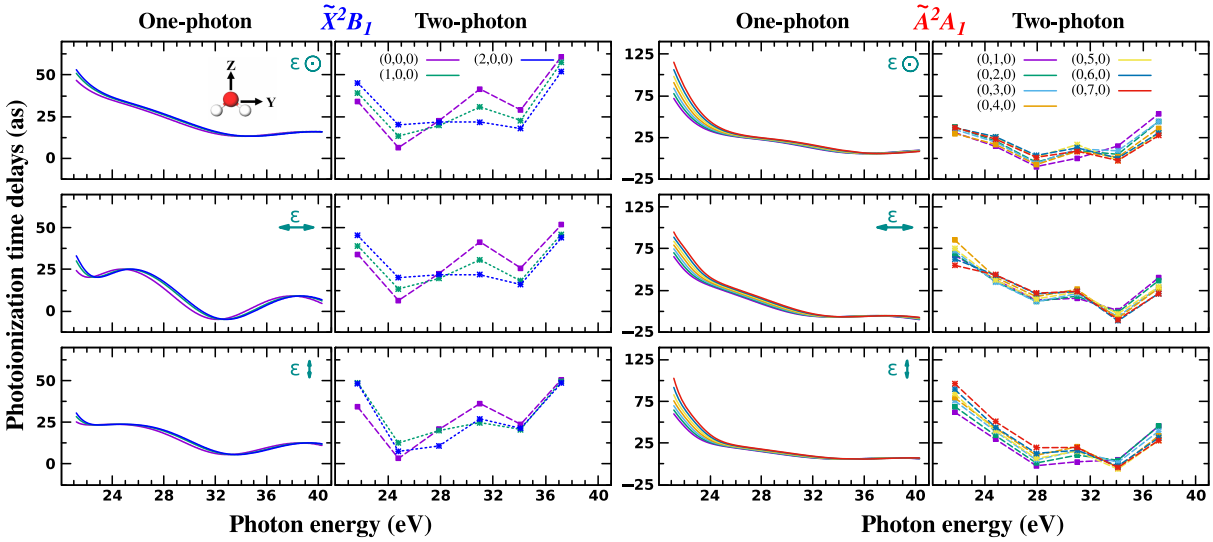

FIG. 4. Vibrationally and channel-resolved one- and two-photon delays for different orientations of the light polarization vector as a function of photon energy. Insets represent the light polarization direction with respect to the molecule.

do not exceed 5 as in the whole photon energy range. The same holds for the one-photon delays that include nuclear motion, although below 23 eV, they increase dramatically as we go down in photon energy, in notorious disagreement with the behavior of the two-photon delays. This implies that continuum-continuum transitions induced by the IR field play a critical role and that this role changes with photon energy in a nonmonotonic way, even at the level of relative delays, where one would expect that the effect of the IR field should cancel out, at least partially.

Figure 4 shows absolute vibrationally resolved one-photon and two-photon ionization delays for the $\tilde{X}^2B_1$ and $\tilde{A}^2A_1$ channels. For a deeper understanding, the delays are given for the three main polarization directions, as defined in the inset of the figure. The corresponding delays for randomly oriented molecules are shown in Fig. 6 of the End Matter. For the one-photon delays, differences between the various vibrational states are only visible at the lower photon energies. We have checked that, in all cases, these differences vanish almost completely when the one-photon delays are plotted as a function of photoelectron energy, indicating that the differences observed at a given photon energy are almost exclusively due to the different velocity of the escaping electron. As the vibrational progression in the $\tilde{A}^2A_1$ channel is rather long and the energy spacing between consecutive bending vibrational states is ~220 meV along the whole progression, differences in the one-photon ionization delays can be as large as ~40 as at the lowest photon energy. This is because at low electron kinetic energies the Coulomb phase shift varies rapidly with energy, so that its energy derivative, hence the one-photon delay, varies even more rapidly with energy [39–42].

The picture is substantially different for the two-photon delays. First, for both the $\tilde{X}^2B_1$ and $\tilde{A}^2A_1$ channels, there is a visible difference between delays associated with different vibrational states all over the investigated photon energy range, typically of not less than ~10 as. Second, the difference between the one- and the two-photon ionization delay, usually called τ_{cc} [39–42], is substantially larger in the $\tilde{X}^2B_1$ channel, where only the symmetric stretching vibrational progression is observed, than in the $\tilde{A}^2A_1$ channel, where only the bending vibrational progression is observed. The largest differences in the $\tilde{X}^2B_1$ channel are found for SB_{20} and SB_{26}, where they can reach up to ~35 as. It can also be observed that, for the $\tilde{A}^2A_1$ channel, the vibrationally resolved one- and two-photon delays exhibit a qualitatively similar, almost monotonic behavior with photon energy, except for SB24. In contrast, for the $\tilde{X}^2B_1$ channel, the behavior of the vibrationally resolved one- and two-photon delays is quite different and nonmonotonic, with one of the delays exhibiting maxima where the other presents a minimum and vice versa. Since τ_{cc} is the time delay associated to the continuum-continuum transitions induced by the IR field, these findings indicate that the IR-photoelectron interaction exhibits pronounced selectivity with respect to the vibrational mode of the remaining molecular cation, i.e., to the specific structural changes associated with each mode.

The origin of this selectivity is intricate and cannot be attributed to a single mechanism. On the one hand, the interaction of the photoelectron with the IR pulse opens additional ionization channels involving partial waves of higher angular momentum, allowing the photoelectron to encounter centrifugal barriers along its path that are absent after absorption of the XUV photon. Depending on the effective height and width of these barriers, which in turn depend on the effective molecular geometry associated with a given vibrational state, the two-photon ionization process may be accelerated or delayed. On the other hand, diffraction patterns arising from the scattering of the photoelectron by multiple atomic center—as predicted

for polyatomic molecules within the fixed-nuclei approximation [43–45]—are naturally sensitive to variations in molecular geometry, and hence to vibrational motion. We show that these effects not only exert a stronger influence on τ_{cc} than on one-photon delays, but also that, despite the vibrational spacings being comparable for the two modes investigated, their impact differs dramatically between them.

In conclusion, we have implemented a theoretical approach that provides time- and vibrationally resolved photoelectron spectra of polyatomic molecules as those expected from high energy resolution RABBIT experiments. The method accounts for all electronic and vibrational degrees of freedom and provides an accurate description of electron correlation. Application to the H_2O molecule shows that the difference between one- and two-photon ionization delays significantly depends on the vibrational mode and the degree of vibrational excitation in the remaining molecular cation. For the $\tilde{X}^2B_1$ channel, where only the symmetric stretching mode can be excited, this difference can be as large ∼35 as, i.e., comparable in magnitude of the measured delays. This is mostly the consequence of a pronounced selectivity of the IR-photoelectron interaction with respect to the specific structural changes associated with each vibrational mode. A similar selectivity on vibrational mode and vibrational excitation is expected for any small and medium-sized polyatomic molecule, which calls for high energy resolution RABBIT experiments able to uncover the effect of molecular vibrations.

Acknowledgments—This work has been supported by the European Research Council (ERC) under the European Union's Horizon 2020 research and innovation programme (Grant agreement No. 951224, TOMATTO) and the Spanish MICINN projects PID2022-138288NB-C31 and PID2022-138288NB-C32. The authors also acknowledge support from the "Severo Ochoa" Programme for Centres of Excellence in R&D (CEX2020-001039-S) and the "María de Maeztu" Programme for Units of Excellence in R&D (CEX2018-000805-M). R. Y. B. acknowledges support from the project ref. SI4/PJI/2024-00243 funded by the Community of Madrid through the direct grant agreement for the encouragement and promotion of research and technology transfer at the Autonomous University of Madrid. All calculations were performed at the Mare Nostrum Supercomputer of the Red Española de Supercomputación (BSC-RES) and the Centro de Computación Científica de la Universidad Autónoma de Madrid (CCC-UAM).

Data availability—The data that support the findings of this article are not publicly available upon publication because it is not technically feasible and/or the cost of preparing, depositing, and hosting the data would be prohibitive within the terms of this research project. The data are available from the authors upon reasonable request.

[1] J. Itatani, F. Quéré, G. L. Yudin, M. Y. Ivanov, F. Krausz, and P. B. Corkum, Phys. Rev. Lett. **88**, 173903 (2002).
[2] E. Goulielmakis, M. Uiberacker, R. Kienberger, A. Baltuska, V. Yakovlev, A. Scrinzi, T. Westerwalbesloh, U. Kleineberg, U. Heinzmann, M. Drescher *et al.*, Science **305**, 1267 (2004).
[3] P.-M. Paul, E. S. Toma, P. Breger, G. Mullot, F. Augé, P. Balcou, H. G. Muller, and P. Agostini, Science **292**, 1689 (2001).
[4] M. Schultze *et al.*, Science **328**, 1658 (2010).
[5] M. Swoboda, T. Fordell, K. Klünder, J. M. Dahlström, M. Miranda, C. Buth, K. J. Schafer, J. Mauritsson, A. L'Huillier, and M. Gisselbrecht, Phys. Rev. Lett. **104**, 103003 (2010).
[6] K. Klünder, J. M. Dahlström, M. Gisselbrecht, T. Fordell, M. Swoboda, D. Guénot, P. Johnsson, J. Caillat, J. Mauritsson, A. Maquet *et al.*, Phys. Rev. Lett. **106**, 143002 (2011).
[7] D. Guénot, D. Kroon, E. Balogh, E. W. Larsen, M. Kotur, M. Miranda, T. Fordell, P. Johnsson, J. Mauritsson, M. Gisselbrecht, K. Varjú, C. L. Arnold, T. Carette, A. S. Kheifets, E. Lindroth, A. L'Huillier, and J. M. Dahlström, J. Phys. B **47**, 245602 (2014).
[8] C. Palatchi, J. M. Dahlström, A. S. Kheifets, I. A. Ivanov, D. M. Canaday, P. Agostini, and L. F. DiMauro, J. Phys. B **47**, 245003 (2014).
[9] M. Kotur, D. Guénot, Á. Jiménez-Galán, D. Kroon, E. W. Larsen, M. Louisy, S. Bengtsson, M. Miranda, J. Mauritsson, C. L. Arnold, S. E. Canton, M. Gisselbrecht, T. Carette, J. M. Dahlström, E. Lindroth, A. Maquet, L. Argenti, F. Martín, and A. L'Huillier, Nat. Commun. **7**, 10566 (2016).
[10] S. Heuser, A. Jiménez Galán, C. Cirelli, C. Marante, M. Sabbar, R. Boge, M. Lucchini, L. Gallmann, I. Ivanov, A. S. Kheifets, J. M. Dahlström, E. Lindroth, L. Argenti, F. Martín, and U. Keller, Phys. Rev. A **94**, 063409 (2016).
[11] M. Isinger, R. J. Squibb, D. Busto, S. Zhong, A. Harth, D. Kroon, S. Nandi, C. L. Arnold, M. Miranda, J. M. Dahlström, E. Lindroth, R. Feifel, M. Gisselbrecht, and A. L'Huillier, Science **358**, 893 (2017).
[12] C. Cirelli *et al.*, Nat. Commun. **9**, 955 (2018).
[13] J. Joseph, F. Holzmeier, D. Bresteau, C. Spezzani, T. Ruchon, J. F. Hergott, O. Tcherbakoff, P. D'Oliveira, J. C. Houver, and D. Dowek, J. Phys. B **53**, 184007 (2020).
[14] L. Barreau, C. L. M. Petersson, M. Klinker, A. Camper, C. Marante, T. Gorman, D. Kiesewetter, L. Argenti, P. Agostini, J. González-Vázquez, P. Salières, L. F. DiMauro, and F. Martín, Phys. Rev. Lett. **122**, 253203 (2019).
[15] S. Luo, R. Weissenbilder, H. Laurell, R. Y. Bello, C. Marante, M. Ammitzböll, L. Neoričić, A. Ljungdahl, R. J. Squibb, R. Feifel, M. Gisselbrecht, C. L. Arnold, F. Martín, E. Lindroth, L. Argenti, D. Busto, and A. L'Huillier, Phys. Rev. Res. **6**, 043271 (2024).
[16] S. Haessler, B. Fabre, J. Higuet, J. Caillat, T. Ruchon, P. Breger, B. Carré, E. Constant, A. Maquet, E. Mével *et al.*, Phys. Rev. A **80**, 011404(R) (2009).
[17] M. Huppert, I. Jordan, D. Baykusheva, A. von Conta, and H. J. Wörner, Phys. Rev. Lett. **117**, 093001 (2016).

[18] D. Baykusheva and H. J. Wörner, J. Chem. Phys. **146**, 124306 (2017).
[19] L. Cattaneo, J. Vos, R. Y. Bello, A. Palacios, S. Heuser, L. Pedrelli, M. Lucchini, C. Cirelli, F. Martín, and U. Keller, Nat. Phys. **14**, 733 (2018).
[20] J. Vos, L. Cattaneo, S. Patchkovskii, T. Zimmermann, C. Cirelli, M. Lucchini, A. Kheifets, A. S. Landsman, and U. Keller, Science **360**, 1326 (2018).
[21] S. Nandi, E. Plésiat, S. Zhong, A. Palacios, D. Busto, M. Isinger, L. Neorivcić, C. L. Arnold, R. J. Squibb, R. Feifel, P. Decleva, A. L'Huillier, F. Martín, and M. Gisselbrecht, Sci. Adv. **6**, eaba7762 (2020).
[22] A. Kamalov, A. L. Wang, P. H. Bucksbaum, D. J. Haxton, and J. P. Cryan, Phys. Rev. A **102**, 023118 (2020).
[23] X. Gong, W. Jiang, J. Tong, J. Qiang, P. Lu, H. Ni, R. Lucchese, K. Ueda, and J. Wu, Phys. Rev. X **12**, 011002 (2022).
[24] S. Heck, M. Han, D. Jelovina, J.-B. Ji, C. Perry, X. Gong, R. Lucchese, K. Ueda, and H. J. Wörner, Phys. Rev. Lett. **129**, 133002 (2022).
[25] L. Cattaneo, L. Pedrelli, R. Y. Bello, A. Palacios, P. D. Keathley, F. Martín, and U. Keller, Phys. Rev. Lett. **128**, 063001 (2022).
[26] H. Ahmadi, E. Plésiat, M. Moioli, F. Frassetto, L. Poletto, P. Decleva, C. D. Schröter, T. Pfeifer, R. Moshammer, A. Palacios, F. Martín, and G. Sansone, Nat. Commun. **13**, 1242 (2022).
[27] V. J. Borràs, J. González-Vázquez, L. Argenti, and F. Martín, Sci. Adv. **9**, eade3855 (2023).
[28] X. Gong, É. Plésiat, A. Palacios, S. Heck, F. Martín, and H. J. Wörner, Nat. Commun. **14**, 4402 (2023).
[29] S. Heck, D. Baykusheva, M. Han, J.-B. Ji, C. Perry, X. Gong, and H. J. Wörner, Sci. Adv. **7**, eabj8121 (2021).
[30] D. Hammerland, T. Berglitsch, P. Zhang, T. T. Luu, K. Ueda, R. R. Lucchese, and H. J. Wörner, Sci. Adv. **10**, eadl3810 (2024).
[31] A. L. Wang, V. V. Serov, A. Kamalov, P. H. Bucksbaum, A. Kheifets, and J. P. Cryan, Phys. Rev. A **104**, 063119 (2021).
[32] V. V. Serov and A. S. Kheifets, J. Chem. Phys. **147**, 204303 (2017).
[33] J. Benda, Z. Mašín, and J. D. Gorfinkiel, Phys. Rev. A **105**, 053101 (2022).
[34] C. M. González-Collado, L. Cattaneo, E. Plésiat, J. J. Omiste, J. Vos, J. González-Vázquez, P. Decleva, U. Keller, A. Palacios, and F. Martín, Phys. Rev. Res. **6**, 033342 (2024).
[35] S. Patchkovskii, J. Benda, D. Ertel, and D. Busto, Phys. Rev. A **107**, 043105 (2023).
[36] D. Ertel, D. Busto, I. Makos, M. Schmoll, J. Benda, H. Ahmadi, M. Moioli, F. Frassetto, L. Poletto, C. D. Schröter, T. Pfeifer, R. Moshammer, Z. Mašín, S. Patchkovskii, and G. Sansone, Sci. Adv. **9**, eadh7747 (2023).
[37] D. Ertel, D. Busto, I. Makos, M. Schmoll, J. Benda, F. Bragheri, R. Osellame, E. Lindroth, S. Patchkovskii, Z. Mašín, and G. Sansone, J. Phys. Chem. A **128**, 1685 (2024).
[38] S. Engin, J. González-Vázquez, G. G. Maliyar, A. R. Milosavljevi, T. Ono, S. Nandi, D. Iablonskyi, K. Kooser, J. D. Bozek, P. Decleva, E. Kukk, K. Ueda, and F. Martín, Struct. Dyn. **6**, 054101 (2019).
[39] J. M. Dahlström, A. L'Huillier, and A. Maquet, J. Phys. B **45**, 183001 (2012).
[40] R. Pazourek, S. Nagele, and J. Burgdörfer, Faraday Discuss. **163**, 353 (2013).
[41] J. Dahlström, D. Guénot, K. Klünder, M. Gisselbrecht, J. Mauritsson, A. L'Huillier, A. Maquet, and R. Taïeb, Chem. Phys. **414**, 53 (2013).
[42] R. Pazourek, S. Nagele, and J. Burgdörfer, Rev. Mod. Phys. **87**, 765 (2015).
[43] E. Plésiat, L. Argenti, E. Kukk, C. Miron, K. Ueda, P. Decleva, and F. Martín, Phys. Rev. A **85**, 023409 (2012).
[44] K. Ueda, C. Miron, E. Plésiat, L. Argenti, M. Patanen, K. Kooser, D. Ayuso, S. Mondal, M. Kimura, K. Sakai, O. Travnikova, A. Palacios, P. Decleva, E. Kukk, and F. Martín, J. Chem. Phys. **139**, 124306 (2013).
[45] E. Plésiat, S. E. Canton, J. D. Bozek, P. Decleva, and F. Martín, J. Phys. Chem. A **123**, 1062 (2019).
[46] R. Y. Bello, R. R. Lucchese, T. N. Rescigno, and C. W. McCurdy, Phys. Rev. Res. **3**, 013228 (2021).
[47] R. Y. Bello, R. R. Lucchese, and C. W. McCurdy, Phys. Rev. A **108**, 033104 (2023).
[48] C. Marante, L. Argenti, and F. Martín, Phys. Rev. A **90**, 012506 (2014).
[49] C. Marante, M. Klinker, I. Corral, J. González-Vázquez, L. Argenti, and F. Martín, J. Chem. Theory Comput. **13**, 499 (2017).
[50] M. Klinker, C. Marante, L. Argenti, J. González-Vázquez, and F. Martín, J. Phys. Chem. Lett. **9**, 756 (2018).
[51] S. M. Poullain, M. Klinker, J. González-Vázquez, and F. Martín, Phys. Chem. Chem. Phys. **21**, 16497 (2019).
[52] R. Y. Bello, V. J. Borràs, J. González-Vázquez, and F. Martín, Phys. Rev. Res. **4**, 043028 (2022).
[53] P. Fernández-Milán, V. J. Borrás, J. González-Vázquez, and F. Martín, J. Chem. Phys. **158**, 134305 (2023).
[54] P. Pranjal, J. González-Vázquez, R. Y. Bello, and F. Martín, J. Phys. Chem. A **128**, 182 (2024).
[55] F. Aquilante *et al.*, J. Comput. Chem. **37**, 506 (2016).
[56] T. H. Dunning, J. Chem. Phys. **90**, 1007 (1989).
[57] R. A. Kendall, T. H. Dunning, and R. J. Harrison, J. Chem. Phys. **96**, 6796 (1992).
[58] J. Cerezo and F. Santoro, J. Comput. Chem. **44**, 626 (2023).

End Matter

Theoretical method: We solve the time-dependent Schrödinger equation (TDSE),

$$\left(\mathcal{H}(\mathbf{r},\mathbf{R},t)-i\frac{\partial}{\partial t}\right)\Psi(\mathbf{r},R,t)=0, \tag{A1}$$

where $\mathbf{r}$ represents all the spin and position coordinates of the electrons, and R denotes all nuclear coordinates (three in the present case). The operator $\mathcal{H}(\mathbf{r},\mathbf{R},t)$ can be partitioned as the sum of the field-free molecular Hamiltonian $\mathcal{H}_0(\mathbf{r},\mathbf{R})$, and the field-molecule interaction potential $V(\mathbf{r},t)$,

$$\mathcal{H}(\mathbf{r},\mathbf{R},t) = \mathcal{H}_0(\mathbf{r},\mathbf{R}) + V(\mathbf{r},t). \tag{A2}$$

The field-free Hamiltonian $\mathcal{H}_0(\mathbf{r},\mathbf{R})$ can be written as the sum of the Born-Oppenheimer electronic Hamiltonian $H_0(\mathbf{r},\mathbf{R})$ and the nuclear kinetic energy operator,

$$\mathcal{H}_0(\mathbf{r},\mathbf{R}) = \hat{T}_N + H_0(\mathbf{r},\mathbf{R}). \tag{A3}$$

The time-dependent wave function in Eq. (A1) is expanded in a basis set of fully correlated adiabatic states [46,47],

$$\begin{aligned}\Psi(\mathbf{r},\mathbf{R},t) = &\sum_b \sum_{v_b} C_{bv_b}(t)\psi_b(\mathbf{r},\mathbf{R})\chi_{v_b}(\mathbf{R})e^{-iE_{bv_b}t} \\ &+ \sum_{\alpha\ell_\alpha m_\alpha} \int d\varepsilon_\alpha \sum_{v_\alpha} C_{\alpha v_\alpha}^{\ell_\alpha m_\alpha \varepsilon_\alpha}(t) \\ &\times \psi_{\alpha\ell_\alpha m_\alpha}^{\varepsilon_\alpha(-)}(\mathbf{r},\mathbf{R})\chi_{v_\alpha}(\mathbf{R})e^{-i(E_{\alpha v_\alpha}+\varepsilon_\alpha)t}.\end{aligned} \tag{A4}$$

In Eq. (A4), $\psi_b(\mathbf{r},\mathbf{R})$ are the bound states of the neutral molecule, and $\psi_{\alpha\ell_\alpha m_\alpha}^{\varepsilon_\alpha(-)}(\mathbf{r},\mathbf{R})$ are electron-ion scattering states or electronic continuum states satisfying the proper asymptotic conditions, namely, incoming spherical waves in all channels and outgoing spherical waves only in channel $\alpha\ell_\alpha m_\alpha$. The labels ε_α and $\ell_\alpha m_\alpha$ represent the asymptotic photoelectron energy and the photoelectron angular momentum quantum numbers. All the electronic states in Eq. (A4) are defined as the eigenfunctions of the Born-Oppenheimer electronic Hamiltonian,

$$\begin{aligned}H_0(\mathbf{r},\mathbf{R})\psi_b(\mathbf{r},\mathbf{R}) &= E_b(\mathbf{R})\psi_b(\mathbf{r},\mathbf{R}) \\ H_0(\mathbf{r},\mathbf{R})\psi_{\alpha\ell_\alpha m_\alpha}^{\varepsilon_\alpha(-)}(\mathbf{r},\mathbf{R}) &= [E_\alpha(\mathbf{R})+\varepsilon_\alpha]\psi_{\alpha\ell_\alpha m_\alpha}^{\varepsilon_\alpha(-)}(\mathbf{r},\mathbf{R}).\end{aligned} \tag{A5}$$

The vibrational states $\chi_{v_b}(\mathbf{R})$ and $\chi_{v_\alpha}(\mathbf{R})$ in Eq. (A4) are the eigenfunctions of the vibrational Hamiltonian for each of the potential energy surfaces of the neutral $E_b(\mathbf{R})$ and ionic $E_\alpha(\mathbf{R})$ electronic states of the molecule.

Computational details: The state energies and dipole couplings between bound-bound, bound-continuum, and continuum-continuum states have been calculated using the XCHEM approach [48,49]. As shown in previous works [27,50–54], XCHEM provides an accurate description of electron correlation for both bound and continuum states. The ground state of water $\tilde{X}^1A_1$ was obtained from a complete active space configuration interaction (CAS-CI) calculation, including the first five a_1, two b_1, and two b_2 orbitals, with the $1a_1$ core orbital always doubly occupied. These orbitals were optimized using the state-average restricted active space SCF (SA-RASSCF) capability of MOLCAS [55], where the ground state of neutral water, $\tilde{X}^1A_1$, and the three lowest states of the corresponding cation, $\tilde{X}^2B_1$, $\tilde{A}^2A_1$, and $\tilde{B}^2B_2$, were included in the state average. We used the cc-pVTZ one-electron basis set [56,57]. The cation states were obtained by constructing the $(N-1)$-electron configuration state functions (CSFs) using the same orbitals obtained in the MOLCAS state average. The first three cation states (energetically open) were included in the close-coupling calculation.

The set of monocentric GABS basis functions [48] used to describe the photoelectron is placed at the system origin, with the B-splines being nonzero for radii $r > R_0$ and the monocentric Gaussians being nonzero for a radii $r < R_1$ such that $R_0 \leq R_1$. The B-splines part of the basis consists of a set of 800 B-splines of order $k = 7$ extending from $R_0 = 7$ a_0 up to $R_{\max} = 400$ a_0 with $\ell \leq 6$. The Gaussian part contains a set of 22 even tempered functions

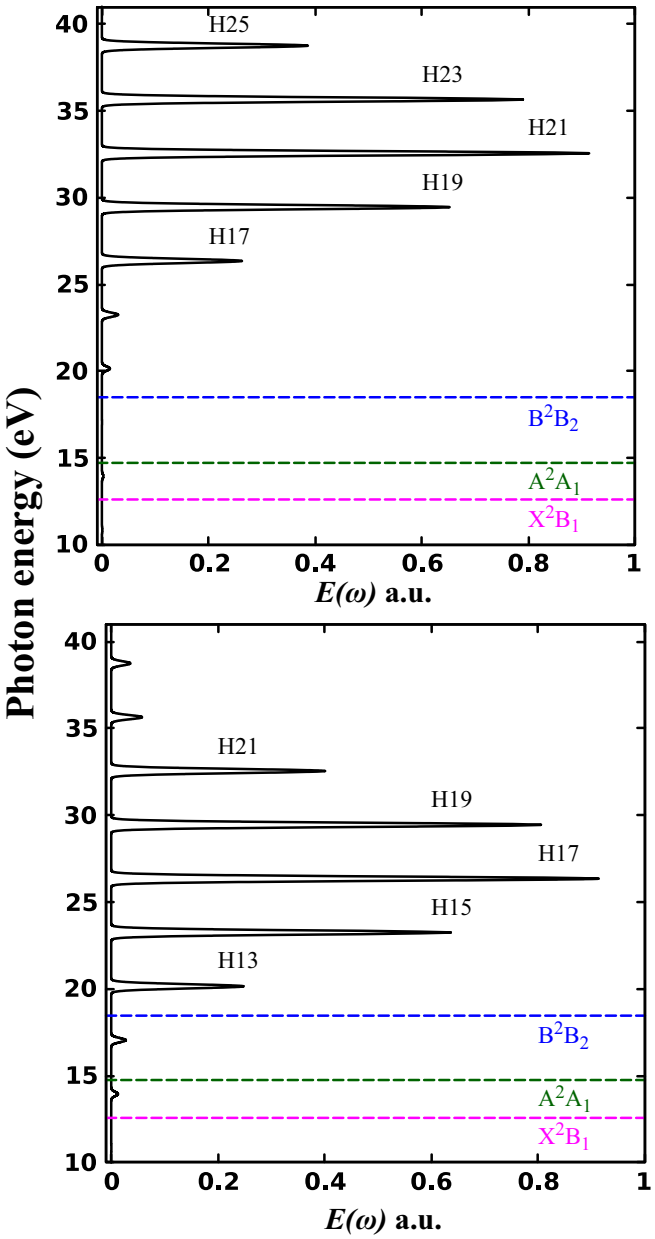

FIG. 5. Spectra of the two APTs used in our calculations. Dashed lines indicate the position of the lowest three ionization thresholds of H_2O.

$G_i^M(r) \propto r^{2\zeta+\ell} e^{-\alpha_i r^2}$, with $\alpha_i = \alpha_0 \beta^i$ ($\alpha_0 = 0.01$, $\beta = 1.46$, $i = 0, 1, \ldots, 21$), and $\zeta = 0$, $\ell \leq 6$.

The three-dimensional vibrational wave functions describing symmetric, antisymmetric, and bending vibrational modes are obtained using the harmonic approximation within the vertical-Hessian approach [58], which has been shown to be a good approximation when all relevant transitions occur in the Franck-Condon (FC) region, as it is the case in the present Letter. Combining all calculated electronic and vibrational states amounts to 118,001 vibronic states in the close-coupling expansion given in Eq. (A4). Although the $\tilde{A}^2A_1$ and $\tilde{X}^2B_1$ states of the cation become degenerate at the linear geometry, leading to the appearance of a rovibronic coupling between them (Renner-Teller effect), such linearization occurs well outside the Franck-Condon (FC) region (see, e.g., Fig. 1 of Ref. [38]), so it is not expected to play a significant role in the present Letter. Dipole matrix elements between vibronic states associated with bound-bound, bound-continuum, and continuum-continuum transitions were evaluated within the FC approximation, which, as shown in [27], is a good approximation when all relevant laser-induced transitions occur in the FC region.

We have used an IR pulse of 30 fs duration, 1.55 eV central frequency, 3×10^{11} W/cm^2 peak intensity, and cosine envelope, and XUV attosecond pulse trains (APTs) of similar duration, cosine envelope, and 10^{12} W/cm^2 peak intensity, in one case containing intense enough harmonics of the IR frequency from H13 to H21 [see Figs. 1(a) and 5(a)] and in another case from H17 to H25 [see Fig. 5(b)]. The two different selections of the APT cover the whole energy range investigated in Ref. [17]. The delay between the APT and the IR was varied between -6 fs and $+6$ fs. The integral over continuum intermediate states in Eq. (A4) is performed over a discrete grid of continuum wave functions [46,47]. In these calculations the energy grid consisted of 2000 points equidistant in energy with spacing $\Delta\varepsilon = 4.0 \times 10^{-4}$ a.u.

Ionization delays for randomly oriented H_2O molecules: Figure 6 shows the vibrationally resolved two-photon ionization delays associated with the symmetric stretching vibrational progression in the $\tilde{X}^2B_1$ channel (left) and the bending vibrational progression in the $\tilde{A}^2A_1$ channel (right) for randomly oriented molecules. They are compared with the corresponding one-photon ionization delays. As can be seen, all conclusions obtained in the main text remain valid for the case in which molecular orientation is not resolved.

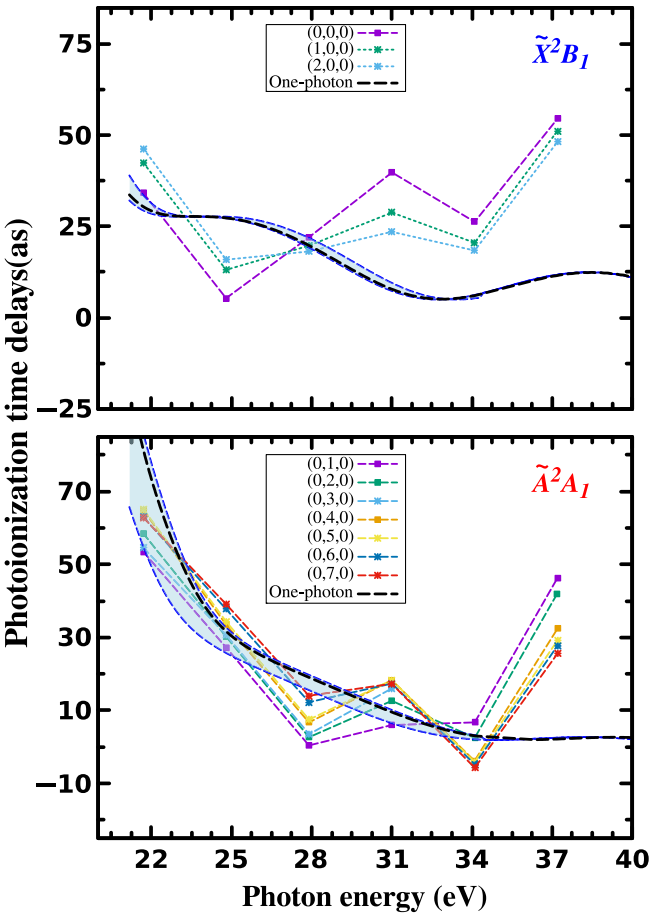

FIG. 6. Vibrationally resolved two-photon ionization delays associated with the symmetric stretching vibrational progression in the $\tilde{X}^2B_1$ channel (up) and the bending vibrational progression in the $\tilde{A}^2A_1$ channel (down) for randomly oriented molecules. The corresponding one-photon ionization delays for the highest and lowest vibrational states are indicated by dashed blue lines. One-photon delays for all other vibrational states lie in the shaded blue region. The vibrationally unresolved one-photon delays are indicated by the black dashed line.